Islamic Azad University

Journal of

Optoelectronical Nanostructures

Winter 2025 / Vol. 6, No. 1

IRANIAN SOLAR ENERGY SCIENTIFIC SOCIETY

Research Paper

Dual-Channel All-Optical Modulator Utilizing Colloidal InSb/SiO_2 Quantum Dot Semiconductor Optical Amplifiers with Enhanced Modulation Depth

Mohammad Faraji [1], Hannaneh Dortaj [*,1] and Samiye Matloub [1]

[1] Quantum and Photonic Research Lab., Faculty of Electrical and Computer Engineering, University of Tabriz, Tabriz, Iran.

Received:
Revised:
Accepted:
Published:

Use your device to scan and read the article online

DOI:

Keywords:
All optical modulator, Modulation depth, Quantum dot, Optical amplifer, Solution-processed.

Abstract:

Quantum dot semiconductor optical amplifiers (QD-SOAs) are promising candidates, yet achieving high modulation depth and gain simultaneously in dual-channel AOMs remains a challenge. Existing studies often focus on single-channel modulation or lack optimization across multiple wavelengths. This paper proposes a dual-channel AOM based on a solution-processed InSb/SiO_2 QD-SOA, designed to modulate and amplify 1.31 and 1.55μm wavelengths simultaneously. A self-consistent solution of the 3D Schrödinger equation is used for modal analysis, while coupled rate and propagation equations evaluate device performance. The results demonstrate nearly 100% modulation depth and gains of 17.94 dB and 17.14 dB at a pump power density of 500 W/cm². These findings highlight the potential of solution-processed QD-SOAs for cost-effective, high-performance optical modulation, addressing key challenges in next-generation optical networks.

Citation: Mohammad Faraji, Hannaneh Dortaj and Samiye Matloub. Dual-Channel All-Optical Modulator Utilizing Colloidal InSb/SiO2 Quantum Dot Semiconductor Optical Amplifiers with Enhanced Modulation Depth. **Journal of Optoelectronical Nanostructures.** 2025; 1 (1): 48-58

***Corresponding author:** Hannaneh Dortaj
Address: Quantum and Photonic Research Lab., Faculty of Electrical and Computer Engineering, University of Tabriz, Tabriz, Iran.
Tell: 00989142409590 **Email:** h_dortaj@tabrizu.ac.ir

1. INTRODUCTION

High-speed signal processing and optical communication technologies largely rely on devices known as all-optical modulators (AOMs), where light is used to modulate light [1], [2], [3]. All-optical signal processing is a promising technology for next-generation high-bit-rate modulation and transparent optical networks thanks to their reduction of deployment expenses and elimination of the bottleneck in ultrafast signal processing by removing the need for costly optical-electrical-optical equipment [4], [5], [6].

Semiconductor optical amplifiers (SOAs) work in a linear and nonlinear method in advanced optical communications systems to achieve a high bit rate and the ability to be integrated [7], [8]. As a linear system, SOA is utilized as an in-line optical amplifier [9]. As a nonlinear system, SOAs have many applications, including cross-gain modulators [10], four-wave mixers [11], cross-phase modulators [12], wavelength conversion [13], logic gates [14], all optical signal processing [15], signal regeneration and switching [16]. However, the utilization of SOAs as intensity modulators [17], [18] has received particular investigation attentiveness in budget-conscious applications such as wavelength division multiplexing passive optical networks (WDM-PONs) [19], [20], [21]. SOAs have a number of prominent advantages, such as low power dissipation, controllable modulation linearity, large-scale monolithic integration capability, low modulation power, full coverage of the entire fiber transmission window, small footprint, and potentially low cost [22]. In addition, SOAs are utilized appropriately as intensity modulators because they can perform the modulation and the amplification simultaneously, and these are an ideal option to increase the speed and efficiency of optical networks [23].

Quantum dot semiconductor optical amplifiers (QD-SOAs) have illustrated a great number of remarkable properties for utilization in numerous applications from all-optical signal processing to optical communication systems [24], [25]. The most salient features enabling their implementation in next-generation high-speed optical access networks include WDM [26], [27], large saturation power [28], potential cost-effectiveness [29], high operation speed [30], patterning-free optical amplification [31], ultrafast gain recovery [32], and the potential for monolithic integration with other optoelectronic devices [33].

A comparison between two structures of SOA intensity modulator and QD-SOA intensity modulator has been accomplished in [34]. In this research, in 60km single mode fiber, the bit rate is 30 (Gb/s) for SOA in 15-24 dBm probe power and 50-200mA bias current and is 32(Gb/s) for QD-SOA in 10-25dBm probe

power and 50-200 bias current. In addition, the gain in the input probe of 10dBm and the bias current of 900mA is about 15dB, and the extinction rate in the structure is 0.55. A structure with three electrodes for injecting bias current is presented for an intensity modulator based on QD-SOA [24]. They reported that this structure solves the nonlinearity defects related to one or two electrode structures. Therefore, at a telecommunication distance of 20-40km with the probe power of -10dBm and the bias current of 300mA, it achieves the bit rate of 35(Gb/s) and the modulation depth of 80%. The saturation gain in this structure is reported 20dB.

Recent advancements in QD-SOA technology and related optical systems have focused on improving modulation depth, bandwidth, and tunability to meet the demands of next-generation optical communications. For instance, optofluidic laser sensors and tunable plasmonic photodetectors in the near-infrared range have demonstrated high sensitivity and efficient light manipulation, highlighting the potential of integrated photonic systems for high-speed signal processing [35]. In this context, graphene-based devices, such as broadband polarization converters, enable dynamic optical control over a wide frequency range, emphasizing the significance of tunable optical components in modern communication networks [36]. Moreover, perovskite metasurfaces have facilitated ultrafast all-optical modulation, achieving an unprecedented signal modulation depth of 2500% with a femtosecond-scale response time, paving the way for high-speed optical computing [37]. Additionally, recent advancements in QD-SOAs have led to the development of polarization-independent designs, such as the polarization-independent quantum dot semiconductor optical amplifier (PIQS) with a fiber-to-fiber gain of 22 dB, addressing critical challenges in optical amplification [38].

Despite these advancements, achieving both high modulation depth and gain simultaneously in dual-channel AOMs based on QD-SOAs remains a major challenge. Most existing studies focus on single-channel modulation, and optimizing modulation performance across multiple wavelengths has yet to be fully realized. Furthermore, the potential of solution-processed quantum dots for enhanced absorption and tunability in dual-channel AOM architectures has not been extensively explored. This research aims to bridge these gaps by introducing a solution-processed $InSb/SiO_2$ QD-SOA structure capable of simultaneously modulating and amplifying two distinct telecommunication wavelengths (1.31 μm and 1.55 μm), providing a practical approach for high-speed optical communication applications.

This paper presents a novel concept for a dual-channel all-optical modulator utilizing QD-SOAs. The proposed device is developed using a solution-processed InSb/SiO2 quantum dot core/shell structure, offering advantages such as enhanced absorption, high efficiency, cost-effective fabrication, room temperature processing, ease of large-area production, and excellent tunability. [39], [40], [41], [42], [43], [44]. For the first time, two different wavelengths within the telecommunication windows have been modulated and amplified simultaneously by applying two pump signals with two different wavelengths of visible range at a high temperature of 300K. Unlike most previous studies, the two-channel AOM based on QD-SOA in this novel approach can be adjusted to modulate and amplify selective wavelengths by tuning QDs' sizes. Moreover, some non-idealities of fabrication conditions have been analyzed in this modulator to propose a practical device. The introduced two-channel AOM is adjusted to absorb two visible wavelengths of 519nm (green) and 663nm (red) and two independent probe signals with wavelengths of 1.31μm and 1.55μm are applied to enable stimulated emission and amplify the modulated signal. This high-speed two-channel AOM based on QD-SOA with a high modulation depth and high optical gain can utilize in several applications, including thermal imaging, signal processing, high-speed computing systems, night vision cameras, wavelength de-multiplexing (WDM), optical communication networks based on dense wavelength division multiplexing (DWDM) technology, free-space communication, online learning systems, and online medical services [21], [45], [46].

2. The Proposed Two-Channel AOM based on QD-SOAs

In this study, two distinct sizes of core/shell QDs, fabricated using the solution process method, have been employed to design a high-contrast all-optical modulator based on QD-SOAs. It has been exploited InSb as the core and SiO2 as the shell to form the absorber layer for the suggested structure. As depicted in Fig. 1(A), laser beams with different wavelengths are used as pump and probe signals, applied through separate channels. Dots with radiuses R1 and R2 are related to channel-1 and channel-2, respectively.

Interband and intersubband transitions between quantized energy levels of the valence band and the conduction band are very considerable in the modulation and amplification process. Two Square pulses, as the information pump signals with the wavelengths of 519nm (green) and 663nm (red), also two continuous waves (CW) as the probe signals with the wavelengths of 1.31μm and 1.55μm (NIR spectra) are applied simultaneously which are adjusted for the QD radiuses

of R1=2.65nm and R2=3.15nm, respectively. By applying pump signals, electrons absorb from the excited state of the valence band (ESv) to the excited state of the conduction band (ESc). Then, the excited electrons descend to the ground state of the conduction band (GSc) rapidly due to the small amount of relaxation time. At the moment, two CW probe signals lead to stimulated emission of electrons from GSc to the ground state of the valence band (GSv) because of the population inversion happened in the conduction band. Eventually, many photons are generated, and the probe signals will be modulated and amplified. The absorption, emission, and recombination process have been demonstrated in Fig. 1 (B). The time constants corresponding to these carrier transition procedures are depicted in Fig. 1(B) as τgev (electron decay time from the GSv to the ESv), τegc (electron decay time from the ESc to the GSc), τgr (carrier lifetime from the GSc to the GSv), τer (carrier lifetime from the ESc to the ESv), the time constants according to FRET mechanism are illustrated as τdown-trans-g(e) (electron transition time from the GSc (ESc) of channel-1 to the GSc (ESc) of channel-2) and τup-trans-g(e) (electron transition time from the GSc (ESc) of channel-2 to the GSc (ESc) of channel-1).

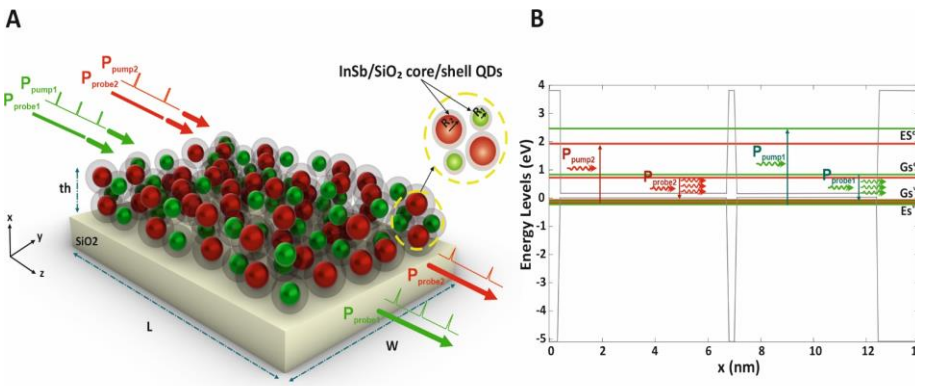

Fig. 1. A) Schematic of two different sizes of QDs arrayed by core/shell InSb/SiO_2 structure. B) The simulated energy band structure of the proposed device by

3. THE THEORETICAL MODELING OF THE PROPOSED STRUCTURE IN THE RATE EQUATION FRAMEWORK

In this section, for modal analysis of two-channel AOM based on QD-SOA, the 3D Schrodinger equation has been solved to achieve eigen-energies,

wavefunctions, and the energy band diagram. Subsequently, to analyze the performance of the two-channel AOM based on QD-SOA and characterize the key metrics of the modulator, the coupled rate and propagation equations are solved. In addition, the impacts of the homogeneous and inhomogeneous broadening and the fluorescence resonance energy transfer (FERT) are involved in coupled rate equations.

By considering the effective mass approximation method and solving the 3D Schrödinger equation by use of the values referred to in Table 1, the energy band diagram of the structure is obtained, as illustrated in Fig. 1(B). Also, eigen-energies and the corresponding wavefunctions of the GSc, ESc, GSv, and ESv have been obtained using the Finite Element Method (FEM) software. The periodic boundary condition is applied for extending the simulated device to the practical system. As Fig. 1(B) displays, the variety between the ESv and ESc in determined QDs is 2.39eV for channel-1 and 1.87eV for channel-2, appropriately adjusted for interband absorption of the pump signals at 519μm (green) and 663μm (red) wavelengths, respectively. Moreover, the variety between the GSc and GSv is 0.94eV for channel-1 and 0.79eV for channel-2, that is proper for the stimulated emission of 1.31μm and 1.55μm wavelengths, respectively. The 3D computed wavefunctions corresponding to each state of the main mode for both channels are similar to our previous work depicted clearly in [47].

TABLE I
MATERIAL PROPERTIES USED IN CALCULATING THE 3D SCHRODINGER EQUATIO [48], [49], [50], [51], [52].

Description	Symbol	Materials	
		InSb	SiO_2
Electron affinity	χ [eV]	4.59	0.95
Bandgap Energy	E_g [eV]	0.17	8.9
Effective mass of the electron	m_e^*	$0.014m_0$	$0.3m_0$
Effective mass of the hole	m_h^*	$0.43m_0$	$0.58m_0$

Due to the restriction of synthesis conditions during the solution process method, the designed exact size of QDs cannot be achieved [45], [53], [54], [55]. Therefore, the non-uniformity of the QDs size will affect the absorption spectra, and the created distribution of energy states is modeled by the Gaussian profile whereat the QDs ensemble is partitioned to 2M + 1 groups of uniform QDs with an energy spacing of ΔE=1meV [29], [56], [57], [58].

$$E_{n,i}^{p} = E_{0,i}^{p} - (M+1-n)\Delta E \quad n = 1,...,2M+1 \quad i = 1,2 \quad p = \text{pump, probe} \tag{1}$$

$$G_i(E_{n,i}^{p}) = \frac{1}{\sqrt{2\pi}\xi_0}\exp\left[\frac{-\left(E_{n,i}^{p} - E_{0,i}^{p}\right)^2}{2\xi_0^{\,2}}\right] \tag{2}$$

here, $E_{0,i}^{p}$ the transfer energy corresponds to the most probable size of QDs (M+1-th QD group), with the index *i* fixed at 1 for channel-1 and 2 for channel-2 The index n refers to the number of active modes, and ξ_0 represents the QD coverage defined as ξ_0 =(1/2.35)FWHM [29], [45].

Furthermore, intrinsic effects such as pressure or temperature lead to interactions between carrier-carrier and phonon-carrier which homogeneously affect all groups, so homogenous broadening will appear on the energy levels. This HB is modeled by a Lorentzian profile with Γ_{HB}=20meV as its FWHM at room temperature [47], [59].

$$B_{m,n}(E_{n,i}^{p} - E_{m,i}^{p}) = \frac{1}{\pi}\frac{\Gamma_{HB}/2}{\left(E_{n,i}^{p} - E_{m,i}^{p}\right)^2 + (\Gamma_{HB}/2)^2} \qquad n = 1,...,2M+1 \tag{3}$$

In consideration of the broadenings acquired, the linear interband absorption coefficient from ES^{v} to ES^{c} arising from applied pump power is attained by [60]:

$$\alpha_{m,n,i}^{Pump} = \frac{2}{V_{QD,i}}\frac{e^2}{c\varepsilon_0 n_i^{pump}\hbar}E_{n,i}^{pump}\,|<\Psi_{e,i}^{v}|\hat{e}.\hat{r}|\Psi_{e,i}^{c}>|^2\, G_i(E_{n,i}^{pump})B_{m,n}(E_{n,i}^{pump} - E_{m,i}^{pump}) \tag{4}$$

Here, c denotes the speed of light in free space, and ε_0 represents the permittivity of free space, n_i^{pump} is the refractive index related to pump wavelengths, ħ is the reduced Planck's constant, *e* is the electron charge, and $V_{QD,i}$ is the volume of the QD. The term $|<\Psi_{e,i}^{v}|\hat{e}.\hat{r}|\Psi_{e,i}^{c}>|$ is the interband transition dipole moment. In final, the total interband absorption is attained through:

$$\alpha_{m,i}^{T}(t) = \int_0^L [\sum_{n=1}^{2M+1}\alpha_{m,n,i}^{pump}(f_{e_{n,i}}^{v}(z,t) - f_{e_{n,i}}^{c}(z,t))]dz \tag{5}$$

Similarly, the gain as a result of the stimulated emission from GS^{c} to GS^{v} by applying probe power is obtained by:

$$g_{m,n,i}^{probe} = \frac{2}{V_{QD,i}}\frac{e^2}{cn_i^{probe}\hbar\varepsilon_0}E_{n,i}^{probe}\,|<\Psi_{g,i}^{c}|\hat{e}.\hat{r}|\Psi_{g,i}^{v}>|^2\, G_i(E_{n,i}^{probe})B_{m,n}(E_{n,i}^{probe} - E_{m,i}^{probe}) \tag{6}$$

Here n_i^{probe} is the refractive index related to probe wavelengths and the term $|<\Psi_{g,i}^{c}|\hat{e}.\hat{r}|\Psi_{g,i}^{v}>|$ is the interband transition dipole moment. In final, the total gain is obtained through:

$$g_{m,i}^{T}(t)=\int_{0}^{L}[\sum_{n=1}^{2M+1}g_{m,n,i}^{probe}(f_{g_{n,i}}^{c}(z,t)-f_{g_{n,i}}^{v}(z,t))]dz \quad (7)$$

On the other hand, Fluorescence (or Förster) resonance energy transfer (FRET) is a non-radiative energy transfer procedure in which a donor (a dot with a smaller radius) transfers the energy to an acceptor (a dot with a larger radius) through dipole-dipole interactions [61]. The transmission rate depends on the distance between two dots and the spectral overlap. In the proposed two-channel AOM based on QD-SOA due to utilizing two distinct groups of QDs, this transfer procedure is assumed as a transmission rate ($W_{12,n}^{l}$) attained through:

$$W_{12,n,i}^{l}=\frac{2}{V_{eff}}\frac{e^2}{\hbar(n_i^p)^2\varepsilon_0}E_{12,n}^{l}|<\Psi_{l,1}^{c}|\hat{e}.\hat{r}|\Psi_{l,2}^{c}>|^2\ B_{m,n}(E_{12,m}^{l}-E_{12,n}^{l})G(E_{12,n}^{l}) \qquad l=GS^c,ES^c \quad (8)$$

Here, V_{eff} is the effective volume of QDs with different sizes, and $E_{12}^{l}=E_{1}^{l}-E_{2}^{l}$. The time constants related to transfer between two different sizes of QDs are computed by $\tau_{up(down)\_trans}^{l}=1/W_{12,n}^{l}$ and involved in coupled rate equations.

4. The Rate and Propagation Equations

The performance of the designed two-channel AOM based on QD-SOA is primarily determined by the dynamics of carriers and photons. For analyzing and modeling, the semiconductor Bloch equation can be used, which provides a more accurate approach for these characteristics. However, in order to avoid the difficulty and time-consuming of calculating the equations, the rate and propagation equations have been solved, and these equations have reported acceptable results. The square pulse train of pump signals and the CW probe signals are propagated along the z-direction. The coupled rate and propagation equations for the proposed structure employing the parameters of Table 2 are represented as:

$$\frac{dn^{c}_{g_{n,2}}(z,t)}{dt}=\frac{n^{c}_{g_{n,1}}(z,t)}{\tau_{down\_trans\_g}}(1-f^{c}_{g_{n,2}}(z,t))-\frac{n^{c}_{g_{n,2}}(z,t)}{\tau_{up\_trans\_g}}(1-f^{c}_{g_{n,1}}(z,t))+\frac{n^{c}_{e_{n,2}}(z,t)}{\tau^{c}_{eg}}(1-f^{c}_{g_{n,2}}(z,t))$$
$$\frac{n^{c}_{g_{n,1}}(z,t)}{\tau_{gr}}(1-f^{v}_{g_{n,1}}(z,t))-\frac{n^{c}_{g_{n,2}}(z,t)}{\tau^{c}_{ge}}(1-f^{c}_{e_{n,2}}(z,t))-\sum_{m=1}^{2M+1}\Gamma Lg_{m,n,2}\frac{P^{probe}_{m,2}(z,t)}{E^{probe}_{m,2}}(f^{c}_{g_{m,2}}(z,t)-f^{v}_{g_{m,2}}(z,t)) \quad (10)$$

$$\frac{dn^{c}_{e_{n,1}}(z,t)}{dt}=-\frac{n^{c}_{e_{n,1}}(z,t)}{\tau_{down\_trans\_e}}(1-f^{c}_{e_{n,2}}(z,t))+\frac{n^{c}_{e_{n,2}}(z,t)}{\tau_{up\_trans\_e}}(1-f^{c}_{e_{n,1}}(z,t))-\frac{n^{c}_{e_{n,1}}(z,t)}{\tau_{er}}(1-f^{v}_{e_{n,1}}(z,t))$$
$$+\frac{n^{c}_{g_{n,1}}(z,t)}{\tau^{c}_{ge}}(1-f^{c}_{e_{n,1}}(z,t))-\frac{n^{c}_{e_{n,1}}(z,t)}{\tau^{c}_{eg}}(1-f^{c}_{g_{n,1}}(z,t))+\sum_{m=1}^{2M+1}\Gamma L\alpha_{m,n,1}\frac{P^{pump}_{m,1}(z,t)}{E^{pump}_{m,1}}(f^{v}_{e_{m,1}}(z,t)-f^{c}_{e_{m,1}}(z,t)) \quad (11)$$

$$\frac{dn^{c}_{e_{n,2}}(z,t)}{dt}=\frac{n^{c}_{e_{n,1}}(z,t)}{\tau_{down\_trans\_g}}(1-f^{c}_{e_{n,2}}(z,t))-\frac{n^{c}_{e_{n,2}}(z,t)}{\tau_{up\_trans\_g}}(1-f^{c}_{e_{n,1}}(z,t))-\frac{n^{c}_{e_{n,2}}(z,t)}{\tau_{er}}(1-f^{v}_{e_{n,2}}(z,t))$$
$$+\frac{n^{c}_{g_{n,2}}(z,t)}{\tau^{c}_{ge}}(1-f^{c}_{e_{n,2}}(z,t))-\frac{n^{c}_{e_{n,2}}(z,t)}{\tau^{c}_{eg}}(1-f^{c}_{g_{n,2}}(z,t))+\sum_{m=1}^{2M+1}\Gamma L\alpha_{m,n,2}\frac{P^{pump}_{m,2}(z,t)}{E^{pump}_{m,2}}(f^{v}_{e_{m,2}}(z,t)-f^{c}_{e_{m,2}}(z,t)) \quad (12)$$

$$\frac{dn^{v}_{g_{n,i}}(z,t)}{dt}=\frac{n^{v}_{e_{n,i}}(z,t)}{\tau^{v}_{eg}}(1-f^{v}_{g_{n.i}}(z,t))-\frac{n^{v}_{g_{n,i}}(z,t)}{\tau^{v}_{ge}}(1-f^{v}_{e_{n.i}}(z,t))$$
$$+\frac{n^{c}_{g_{n.i}}(z,t)}{\tau_{gr}}(1-f^{v}_{g_{n.i}})+\sum_{m=1}^{2M+1}\Gamma Lg_{m,n,i}\frac{P^{probe}_{m,i}(z,t)}{E^{probe}_{m,i}}(f^{c}_{g_{m,i}}(z,t)-f^{v}_{g_{m,i}}(z,t)) \quad (13)$$

$$\frac{dn^{v}_{e_{n,i}}(z,t)}{dt}=\frac{n^{v}_{g_{n,i}}(z,t)}{\tau^{v}_{ge}}(1-f^{v}_{e_{n.i}}(z,t))-\frac{n^{v}_{e_{n,i}}(z,t)}{\tau^{v}_{eg}}(1-f^{v}_{g_{n.i}}(z,t))$$
$$+\frac{n^{c}_{e_{n.i}}(z,t)}{\tau_{er}}(1-f^{v}_{e_{n.i}}(z,t))-\sum_{m=1}^{2M+1}\Gamma L\alpha_{m,n,i}\frac{P^{pump}_{m,1}(z,t)}{E^{pump}_{m,1}}(f^{v}_{e_{m,1}}(z,t)-f^{c}_{e_{m,1}}(z,t)) \quad (14)$$

$$\frac{\partial P^{pump}_{m,i}(z,t)}{\partial z}=(-\sum_{n=1}^{2M+1}\Gamma\alpha_{m,n,i}(f^{v}_{e_{n,i}}(z,t)-f^{c}_{e_{n,i}}(z,t))-\alpha_{\text{int}})P^{pump}_{m,i}(z,t) \quad (15)$$

$$\frac{\partial P^{probe}_{m,i}(z,t)}{\partial z}=(\sum_{n=1}^{2M+1}\Gamma g_{m,n,i}(f^{c}_{g_{n,i}}(z,t)-f^{v}_{g_{n,i}}(z,t))-\alpha_{\text{int}})P^{probe}_{m,i}(z,t) \quad (16)$$

Where $n^{c}_{g_{n,i}}$, $n^{c}_{e_{n,i}}$, $n^{v}_{g_{n,i}}$, and $n^{v}_{e_{n,i}}$ are the number of electrons in GS^{c}, ES^{c}, GS^{v}, and ES^{v}, respectively. Additionally, $P^{pump}_{m,i}$ and $P^{probe}_{m,i}$ are the optical pump power and the CW probe power, respectively. The corresponding carrier occupation probabilities are illustrated as $f^{c}_{g_{n.i}}$, $f^{c}_{e_{n.i}}$, $f^{v}_{g_{n.i}}$, and $f^{v}_{e_{n.i}}$, respectively. Additionally, the number of electrons corresponding to their respective occupation probabilities are calculated by

$n_{g_{n,i}}^{c(v)}(z,t) = f_{g_{n,i}}^{c(v)}(z,t)N_{G_i}^{c(v)}$, $n_{e_{n,i}}^{c(v)}(z,t) = f_{e_{n,i}}^{c(v)}(z,t)N_{E_i}^{c(v)}$. All the time constants are explained in detail in Section 2. Furthermore, the time constants related to the electron escape process in the valence and the conduction bands are acquired as:

$$\tau_{ge}{}^{c(v)} = \tau_{eg}{}^{c(v)} \frac{D_g^{c(v)}}{D_e^{c(v)}} \exp(\Delta E_{eg}{}^{c(v)} / KT) \tag{17}$$

where $\Delta E_{eg}^{c(v)}$ is the energy interval between ES$^{c(v)}$ and GS$^{c(v)}$ [65], [66], [67]. Degeneracies are determined by $D_g^c = 1$, $D_e^c = 3$, $D_g^v = 1$, and $D_e^v = 3$. The total number of electrons of each state, GS^c, ES^c, GS^v, and ES^v are demonstrated with $N_{G_i}^{c(v)} = N_{QD,i}V_d D_g^{c(v)}$, $N_{E_i}^{c(v)} = N_{QD,i}V_d D_e^{c(v)}$, in which $N_{QD,i}$ is the density of QDs and V_d is the volume of the active region for both channels.

TABLE Ⅱ

The Parameters required in calculating rate and propagation equations [62], [63], [64].

Parameters	Channel-1	Channel-2
Radius of QD [nm]	R_1=2.65	R_2=3.15
L [μm]	300	
W [μm]	300	
th [μm]	60	
QD volume density (NQD) [cm^{-3}]	0.5×10^9	0.5×10^9
The optical confinement factor (Γ)	0.004	0.002
Refractive index	Pump: 4.0132	Pump: 5.0034
	Probe: 4.0188	Probe: 3.9637
The electron relaxation time from the ES^c to the GS^c ($\tau_{eg}{}^c$) [ps]	1	
The electron relaxation time from the GS^v to the ES^v ($\tau_{ge}{}^v$) [ps]	1	
The electron recombination time from the ES^c to the ES^v (τ_{er}) [ps]	10	
The electron recombination time from the GS^c to the GS^v (τ_{gr}) [ps]	10	

5. SIMULATION RESULTS

In this section, the performance of the proposed two-channel AOM based on QD-SOA has been determined by evaluating the coupled rate and propagation equations (9-16) according to the parameters referred in Table2. The most critical metrics in the characteristics of an intensity modulator based on SOA are the gain

and modulation depth (MD). So, these parameters are achieved, and the effects of some non-idealities of fabrication condition on the performance of the structure are investigated as follow.

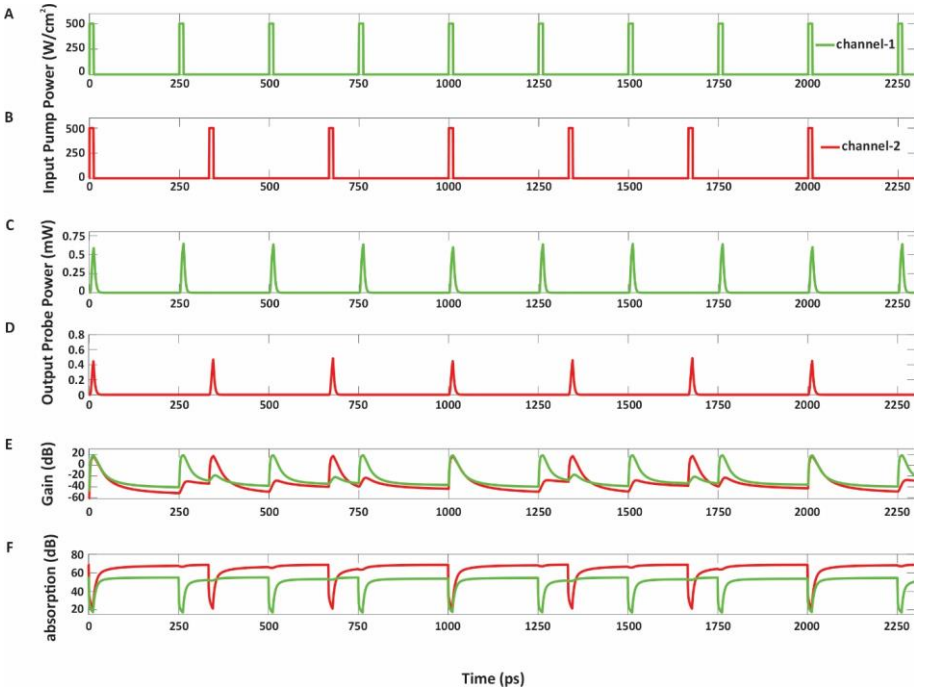

Fig. 2. A) Applied pump power signals with the frequencies of 3GHz for channel-1 and B) 4GHz for channel-2. C) Output modulated probe power signals as a function of time for channel-1 and D) for channel-2. E) Calculated gain versus time for both channels. F) Calculated linear absorption versus time for both channels.

According to Fig. 1(A, B), two square pump power signals with different frequencies have been applied for each channel. In order to explain the synchronicity and asynchrony of the activation of the channels, the output modulated probe power have been represented in Fig. 2(C, D). Channel-1 (smaller QD) has a frequency of 3GHz, and channel-2 (larger QDs) has a frequency of 4GHz. As the results show in Fig. 2(E, F), when the pump power is applied to just one channel, in the gain and the absorption profile, the value of the channel with zero input power has moved away from its stable state, which indicates that the two channels are correlated to each other because of the FRET mechanism.

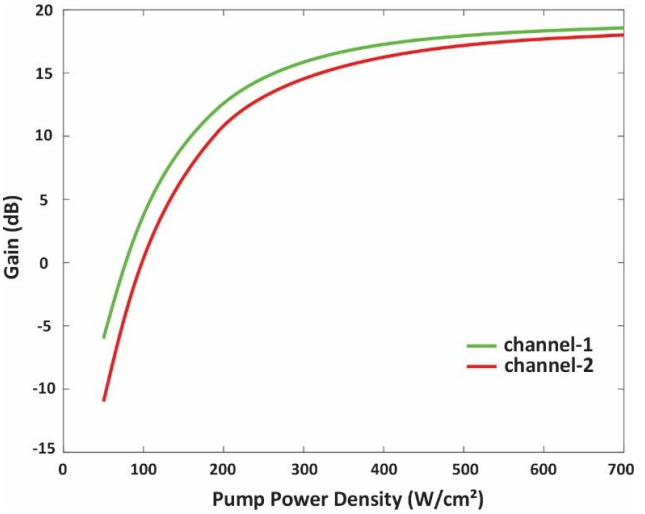

Fig. 3. The gain profile versus the pump power density for both channels at the probe power of -20dBm.

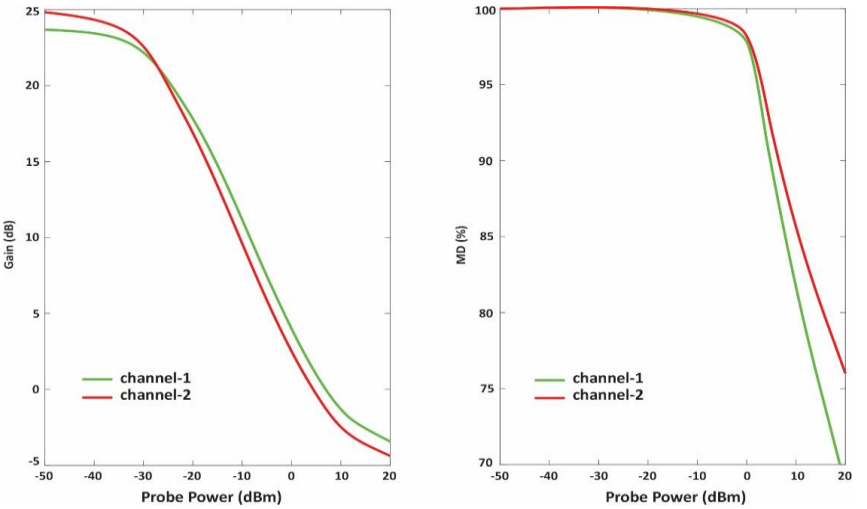

Fig. 4. A) Gain of the proposed device as a function of probe power for both channels. B) MD of the proposed device as a function of probe power for both channels.

Due to the increase in input pump density for the fixed probe power value of -20dB, it is expected that the gain will ascend because of the enhancement in

carrier absorption from the valence band to the conduction band, which causes an increment in excited carriers in the conduction band. Increasing carriers in ES^c leads to increasing in the stimulated emission in the presence of the probe power and thus increases the gain. Furthermore, as the pump power density increases, the gain increases until ES^c is not saturated with excited carriers. As seen in Fig. 3, with the increase of the pump power density up to 500W/cm^2, the gain changes almost linearly. From this value onwards, as the pump power density increases, the changes in the output gain are small, which shows the saturation of ES^c. As a result, the output probe power and the gain will be stable at high pump power densities.

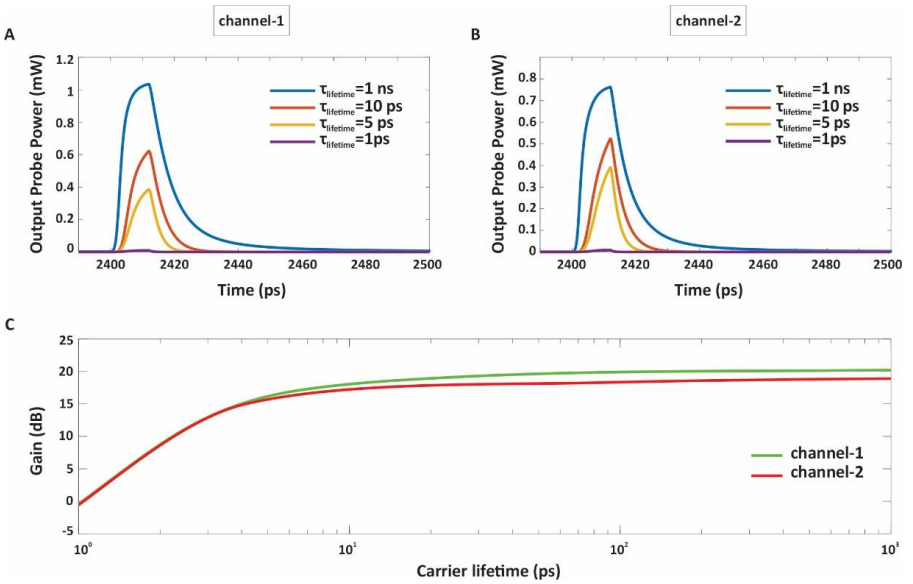

Fig. 5. Output probe power versus time for different values of carrier lifetime A) for channel-1 and B) for channel-2. C) The gain of the device as a function of carrier lifetime.

Fig. 4(A) displays the saturation of the gain in low probe power values, and it indicates that with increasing the input probe power, the gain goes out of the saturated state (linear) and moves to the nonlinear state. For amplification, probe powers that are specific to the saturation regime are used, and for signal processing, probe powers that are greater than the saturation input probe power of 3dB are utilized. It can also be realized that up to the probe power of 0dBm, this structure with a pump power density of 500W/cm^2 is still able to amplify the input

probe power. The saturated gain in this structure is 23.6dB and 24.8 dB for channel-1&2, respectively. Fig. 4(B) represents the modulation depth (MD) as a function of the input probe power, which can be concluded that until the probe power of 20dBm MD has a suitable value after that, it reduces by increasing the probe power.

One of the parameters that affect the gain of the device is the carrier recombination time. This parameter is completely dependent on the conditions of QDs' fabricating process. Due to the presence of traps that modify the recombination process time, it is possible to control the recombination time by engineering the construction of these QDs. Fig. 5(A, B) shows the output probe power in different carrier lifetimes for channel-1&2 which indicates that by increasing the lifetime, the output probe power increases. This is because with the increase of lifetime, the probability of spontaneous emission of electrons decreases. As a result, the noise arising from the creation of unwanted photons from spontaneous emission is reduced. In this case, there will be more time and more carriers to perform stimulated emission by applying the probe signal. Fig. 5(C) illustrates the gain variation with respect to the different lifetimes, and it indicates that the gain converges as the lifetime increases from 1ps to 1ns. The life time in all simulations is fixed for the optimal value of 10ns.

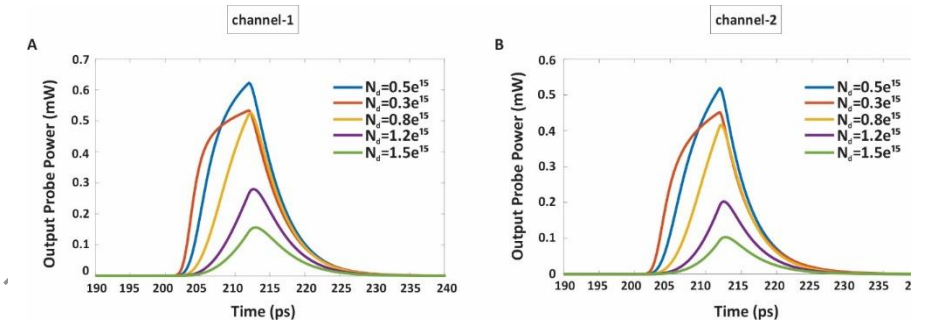

Fig. 6. Output probe power versus time for different values of N_ds A) for channel-1 and B) for channel-2.

Another parameter that affects the gain are the volume density of QDs (Nd) which depends on the QDs synthesis process. According to Fig. 6(A, B), it can be emphasized that for both channels, the amount of N_d should not be more or less than a value, which directly affects the gain and subsequently reduces the output probe power. According to this figure, the gain has the maximum value in

$N_d=0.5\times10^{15}$ for both channels.

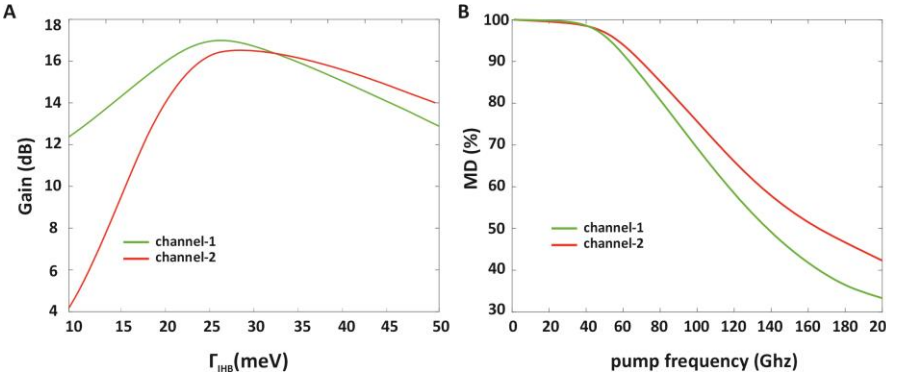

Fig. 7. A) Calculated gain as a function of Γ_{IHB} for channel-1 and channel-2. B) MD has been reduced by increasing the pump frequency for both channels.

On the other hand, Γ_{IHB} defined as the FWHM of the non-uniform distribution of QDs also affects the gain of the proposed device. Fig. 7(A) indicates that with the increase of Γ_{IHB} up to 25meV, the gain increases for both channels, and then with a further increase of Γ_{IHB} a decrease in the gain can be observed. In addition to the gain has its maximum value when Γ_{IHB}=25meV, another point is that this amount of FWHM in the inhomogeneous broadening does not cause a lot of complexity and difficulty in the synthesis and construction of this device, and this is very valuable.

In the end, the effect of changes in the input pump frequency on the MD is depicted in Fig. 7(B) for both channels. Given that with the increase in the frequency, the carriers have little chance to recover themselves and return to a stable state; therefore, the MD, which is defined as the distance between the ON and OFF state at the output, is reduced. In other words, at high frequencies, some carriers exist in the conduction band even when the pump power is not present, which causes a gain when the pump power is OFF. Eventually, the distance between the ON and OFF state in the output probe power is reduced, and thus, the MD is reduced.

The structural parameters of the proposed dual-channel AOM were carefully selected based on quantum confinement effects, optical absorption characteristics, and practical telecommunication standards. The quantum dot (QD) radii (R_1 = 2.65 nm, R_2 = 3.15 nm) were determined by solving the 3D Schrödinger equation, ensuring that their absorption peaks align with the chosen pump wavelengths (519 nm, 663 nm) and their emission matches the telecommunication probe wavelengths (1.31 μm, 1.55 μm). These wavelengths were selected to maximize

optical gain and modulation efficiency while maintaining compatibility with standard fiber-optic systems. Additionally, the pump power density (500 W/cm²) was optimized through numerical simulations of coupled rate and propagation equations to achieve high modulation depth (~100%) and gain (~17.94 dB and 17.14 dB).

Fabrication imperfections introduce slight variations in structural parameters [68]. To assess the robustness of the proposed AOM, we analyzed its sensitivity to deviations in key design values. A ±5% change in QD radius results in less than a 1% shift in absorption/emission wavelengths, ensuring stable operation. The device also tolerates pump power fluctuations of ±10% with minimal impact on gain (~1 dB variation) and maintains >90% modulation depth. Additionally, a ±5 nm misalignment in pump or probe wavelengths leads to only a ~5% reduction in modulation depth, demonstrating the flexibility of the proposed structure. These findings confirm that the device remains functional under realistic fabrication constraints, making it feasible for experimental implementation.

6. CONCLUSION

In this study, a new conception of a two-channel AOM employing the colloidal InSb/SiO2 structure based on QD-SOAs with the solution process method is introduced. The proposed structure is suggested to modulate and amplify two distinct wavelengths of telecommunication windows (1.31μm, 1.55 μm) simultaneously by applying two pump signals with two different wavelengths of the visible range (519nm, 663nm) through two separate channels. For modal analysis of the designed two-channel AOM based on QD-SOAs 3D Schrodinger equation has been solved, and to appraise the theoretical analysis the coupled rate and propagation equations have been calculated. From the simulation results, it can be accomplished that the modulation depth is obtained 100 % and the gain is about 17.94 dB and 17.14 dB in the pump power density 500W/cm^2 and probe power -20dBm for channel-1 and channel-2, respectively.

7. REFERENCES

[1] D. Pacifici, H. J. Lezec and H. A. Atwater. *All-optical modulation by plasmonic excitation of CdSe quantum dots*. Nat. Photonics. vol. 1, no. 7. (Jul. 2007). pp. 402–406. doi: 10.1038/nphoton.2007.95.

[2] C. Husko, A. De Rossi, S. Combrié, Q. V. Tran, F. Raineri, and C. W. Wong. *Ultrafast all-optical modulation in GaAs photonic crystal cavities*. Appl. Phys. Lett. vol. 94, no. 2. (Jan. 2009). doi: 10.1063/1.3068755.

[3] H. Takeda. *All-optical modulation and amplification resulting from*

population inversion in two-level systems using a photonic-crystal cavity. Phys. Rev. A. vol. 86, no. 1. (Jul. 2012). p. 013803. doi: 10.1103/PhysRevA.86.013803.

[4] Xiang Zhou and Jianjun Yu. *Multi-Level, Multi-Dimensional Coding for High-Speed and High-Spectral-Efficiency Optical Transmission*. J. Light. Technol. vol. 27, no. 16. (Aug. 2009). pp. 3641–3653. doi: 10.1109/JLT.2009.2022765.

[5] P. J. Winzer and R.-J. Essiambre. *Advanced optical modulation formats*. in Optical Fiber Telecommunications *VB*, Elsevier. (2008). pp. 23–93. [Online]. Available: https://www.sciencedirect.com/science/article/abs/pii/B9780123741721000023

[6] Y. Z. Yueying Zhan, M. Z. Min Zhang, M. L. Mintao Liu, L. L. Lei Liu, and X. C. Xue Chen. *All-optical format conversion of NRZ-OOK to QPSK and 16QAM signals via XPM in a SOA-MZI*. Chinese Opt. Lett. vol. 11, no. 3. (2013). pp. 030604–030607. doi: 10.3788/COL201311.030604.

[7] C. Politi, D. Klonidis, and M. J. O'Mahony. *Dynamic Behavior of Wavelength Converters Based on FWM in SOAs*. IEEE J. Quantum Electron. vol. 42, no. 2, pp. 108–125. (Feb. 2006). doi: 10.1109/JQE.2005.861822.

[8] A. Ghaderi. *Simulation of Gain in Semiconductor Optical Amplifier Tension*. Majlesi J. Telecommun. Devices. vol. 4, no. 4, (2015), [Online]. Available: https://sanad.iau.ir/en/Article/901596

[9] T. Matsumoto et al. *In-line Optical Amplification for Silicon Photonics Platform by Flip-Chip Bonded InP-SOAs*. in 2018 Optical Fiber Communications Conference and Exposition OFC 2018 - *Proceedings*, Optical Society of America. (2018). pp. 1–3. [Online]. Available: https://opg.optica.org/abstract.cfm?uri=ofc-2018-Tu2A.4

[10] S. Bloch, A. Lifshitz, E. Granot, and S. Sternklar. *Wavelength monitoring with mutually modulated cross-gain modulation in a semiconductor optical amplifier and Brillouin amplifier*. J. Opt. Soc. Am. *B*. vol. 30, no. 4. (Apr. 2013). p. 974, doi: 10.1364/JOSAB.30.000974.

[11] P. D. Lakshmijayasimha, A. Kaszubowska-Anandarajah, E. P. Martin, P. Landais, and P. M. Anandarajah. *Expansion and phase correlation of gain-switched optical frequency combs through FWM in an SOA*. in Optics InfoBase Conference Papers, Optica Publishing Group. (2019). pp. W1B-2. [Online]. Available: https://opg.optica.org/abstract.cfm?uri=OFC-2019-W1B.2

[12] M. Syuhaimi Ab-Rahman and A. H. Almabrok Swedan. *Semiconductor optical amplifier for optical channel capacity improvement based on cross-phase modulation*. J. Telecommun. Electron. Comput. Eng. vol. 10, no. 1–5.

(2018). pp. 89–95. [Online]. Available: https://jtec.utem.edu.my/jtec/article/view/3637
[13] S. R, S. R. A, S. S, and E. M. K. *Cross polarization modulation based wavelength conversion with very low pump power in SOA: An investigation*. Optik (Stuttg). vol. 185. (May 2019). pp. 852–858, doi: 10.1016/j.ijleo.2019.04.016.
[14] H. Hu, X. Zhang, and S. Zhao. *High-speed all-optical logic gate using QD-SOA and its application*. Cogent Phys. vol. 4, no. 1. (Jan. 2017). p. 1388156. doi: 10.1080/23311940.2017.1388156.
[15] A. Kotb and C. Guo. *All-optical multifunctional AND, NOR, and XNOR logic gates using semiconductor optical amplifiers*. Phys. Scr. vol. 95 no. 8. (2020). p. 85506, [Online]. Available: https://iopscience.iop.org/article/10.1088/1402-4896/aba057/meta
[16] V. Sasikala and K. Chitra, *All optical switching and associated technologies: a review*. J. Opt. vol. 47, no. 3. (Sep. 2018). pp. 307–317. doi: 10.1007/s12596-018-0452-3.
[17] S.-J. Park, G.-Y. Kim, and T.-S. Park. *WDM-PON system based on the laser light injected reflective semiconductor optical amplifier*. Opt. Fiber Technol. vol. 12, no. 2. (2006). pp. 162–169. [Online]. Available: https://www.sciencedirect.com/science/article/abs/pii/S1068520005000398
[18] H. Takesue and T. Sugie. *Wavelength channel data rewrite using saturated SOA modulator for WDM networks with centralized light sources*. J. Light. Technol. vol. 21, no. 11. (2003). pp. 2546. [Online]. Available: https://opg.optica.org/jlt/abstract.cfm?uri=JLT-21-11-2546
[19] F. El-Nahal and N. Hanik. *Technologies for future wavelength division multiplexing passive optical networks*. IET Optoelectron. vol. 14, no. 2. (Apr. 2020). pp. 53–57. doi: 10.1049/iet-opt.2018.5056.
[20] J. L. Wei, A. Hamié, R. P. Giddings, and J. M. Tang. *Semiconductor optical amplifier-enabled intensity modulation of adaptively modulated optical OFDM signals in SMF-based IMDD systems.* J. Light. Technol. vol. 27, no. 16. (2009) pp. 3678–3688.. [Online]. Available: https://opg.optica.org/jlt/abstract.cfm?uri=JLT-27-16-3678
[21] V. Fallahi and M. Seifouri. *Novel four-channel all optical demultiplexer based on square PhCRR for using WDM applications*. J. Optoelectron. Nanostructures. vol. 3, no. 4. (2018). pp. 59–70 [Online]. Available: https://sanad.iau.ir/en/Article/1182771
[22] Z. V Rizou and K. E. Zoiros. *Semiconductor optical amplifier dynamics and pattern effects.* in Handbook of Optoelectronic Device Modeling and Simulation, CRC Press. (2017). pp. 771–796. [Online]. Available: https://www.taylorfrancis.com/chapters/edit/10.1201/9781315152301-

25/semiconductor-optical-amplifier-dynamics-pattern-effects-zoe-rizou-kyriakos-zoiros
[23] E. Udvary and T. Berceli, "Improvements in the linearity of semiconductor optical amplifiers as external modulators," *IEEE Trans. Microw. Theory Tech.*, vol. 58, no. 11, pp. 3161–3166, 2010, [Online]. Available: https://ieeexplore.ieee.org/abstract/document/5585845/
[24] H. A. Yazbeck, V. V Belyaev, I. M. Tkachenko, and M. M. Hamze. *Multi-electrode quantum-dot semiconductor optical amplifier as an intensity modulator of signals in optical communication systems*. J. Phys. Conf. Ser. vol. 1560, no. 1. (Jun. 2020). pp. 012021. doi: 10.1088/1742-6596/1560/1/012021.
[25] A. Farmani and M. H. Sheikhi. *Quantum-dot semiconductor optical amplifier: performance and application for optical logic gates*. Majlesi J. Telecommun. Devices. vol. 6, no. 3. (2017). pp. 93–97. [Online]. Available: https://sanad.iau.ir/en/Article/901395
[26] F. Hakimian, M. R. Shayesteh, and M. Moslemi. *A Proposal for a New Method of Modeling of the Quantum Dot Semiconductor Optical Amplifiers*. J. Optoelectron. Nanostructures. vol. 4, no. 3. (2019). pp. 1–16. [Online]. Available: https://sanad.iau.ir/en/Article/1182634
[27] Y. Shahamat and M. Vahedi. *Design and Simulation of a Waveguide Division De-multiplexer (DWDM) for Communication Application*. Majlesi J. Telecommun. Devices. vol. 8, no. 1. (2019). pp. 1–5. [Online]. Available: https://sanad.iau.ir/en/Article/901591
[28] T. W. Berg, S. Bischoff, I. Magnusdottir, and J. Mork. *Ultrafast gain recovery and modulation limitations in self-assembled quantum-dot devices*. IEEE Photonics Technol. Lett. vol. 13, no. 6. (2001). pp. 541–543. [Online]. Available: https://ieeexplore.ieee.org/abstract/document/924013/
[29] H. G. Yousefabad, S. Matloub, and A. Rostami. *Ultra-broadband Optical Gain Engineering in Solution-processed QD-SOA Based on Superimposed Quantum Structure*. Sci. Rep. vol. 9, no. 1. (Sep. 2019). p. 12919. doi: 10.1038/s41598-019-49369-6.
[30] Y. Ben Ezra, B. I. Lembrikov, and P. Choudhury. *Quantum dot-semiconductor optical amplifiers (QD-SOA): dynamics and applications*. in Optical Amplifiers-A Few Different Dimensions, IntechOpen. (2018). pp. 10–38. [Online]. Available: https://www.intechopen.com/chapters/59750
[31] A. Marculescu. *Semiconductor optical amplifiers: modeling, signal regeneration and conversion*. ETH Zurich. (2018). [Online]. Available: https://www.research-collection.ethz.ch/handle/20.500.11850/272998
[32] K. Komatsu, G. Hosoya, and H. Yashima. *Ultrafast all-optical digital comparator using quantum-dot semiconductor optical amplifiers*. Opt.

Quantum Electron. vol. 51, no. 2. (2019). pp. 1–16. [Online]. Available: https://link.springer.com/article/10.1007/s11082-019-1756-5

[33] B. Boriboon *et al. Performances of Conventional SOAs Versus QD-SOA in 1530-nm Upstream Transmission of 40 Gb/s Access Network*. IEEE Photonics J. vol. 14, no. 1. (2021). pp. 1–12. [Online]. Available: https://ieeexplore.ieee.org/abstract/document/9664304/

[34] A. Hamié, M. Hamze, J. L. Wei, A. Sharaiha, and J. M. Tang. *Theoretical investigations of quantum-dot semiconductor optical amplifier enabled intensity modulation of adaptively modulated optical OFDM signals in IMDD PON systems*. Opt. Express. vol. 19, no. 25. (Dec. 2011). p. 25696. doi: 10.1364/OE.19.025696.

[35] M. H. Mozaffari and A. Farmani. *On-Chip Single-Mode Optofluidic Microresonator Dye Laser Sensor*. IEEE Sens. J. vol. 20, no. 7. (Apr. 2020). pp. 3556–3563. doi: 10.1109/JSEN.2019.2962727.

[36] E. Khosravian, H. R. Mashayekhi, and A. Farmani. *Tunable plasmonics photodetector in near-infrared wavelengths using graphene chemical doping method*. AEU - Int. J. Electron. Commun. vol. 127. (Dec. 2020). p. 153472. doi: 10.1016/j.aeue.2020.153472.

[37] M. A. Masharin, T. Oskolkova, F. Isik, H. Volkan Demir, A. K. Samusev, and S. V Makarov. *Giant Ultrafast All-Optical Modulation Based on Exceptional Points in Exciton–Polariton Perovskite Metasurfaces*. ACS Nano. vol. 18, no. 4. (Jan. 2024). pp. 3447–3455. doi: 10.1021/acsnano.3c10636.

[38] A. Farmani, M. Farhang, and M. H. Sheikhi. *High performance polarization-independent Quantum Dot Semiconductor Optical Amplifier with 22 dB fiber to fiber gain using Mode Propagation Tuning without additional polarization controller*. Opt. Laser Technol. vol. 93. (Aug. 2017). pp. 127–132. doi: 10.1016/j.optlastec.2017.02.007.

[39] S. Matloub, P. Amini, and A. Rostami. *Switchable Multi-color Solution-processed QD-laser*. Sci. Rep. vol. 10, no. 1. (2020). pp. 1–14. [Online]. Available: https://www.nature.com/articles/s41598-020-60859-w

[40] H. Dortaj *et al. High-speed and high-precision PbSe/PbI2 solution process mid-infrared camera*. Sci. Rep. vol. 11, no. 1. (Jan. 2021). p. 1533. doi: 10.1038/s41598-020-80847-4.

[41] H. Dortaj and S. Matloub. *Two-wavelength Quantum Dot Mid-Infrared Photodetectors Using Solution Process Method*. in 2023 5th Iranian International Conference on Microelectronics (IICM), IEEE. (2023). pp. 31–35. [Online]. Available: https://ieeexplore.ieee.org/abstract/document/10443151/

[42] H. Dortaj and S. Matloub. *Design and simulation of two-color mid-infrared*

photoconductors based on intersubband transitions in quantum structures. Phys. E Low-dimensional Syst. Nanostructures. (Jan. 2023). p. 115660. doi: https://doi.org/10.1016/j.physe.2023.115660.

[43] H. Dortaj, S. Matloub, and H. Baghban. *Design and characterization of colloidal quantum dot photoconductors for multi-color mid-infrared detection*. Opt. Laser Technol. vol. 180. (2025). p. 111493. [Online]. Available: https://www.sciencedirect.com/science/article/pii/S0030399224009514

[44] M. Faraji, S. Matloub, and H. Dortaj. *Simulation and Fabrication Feasibility of Two-Channel All-optical Modulator Exploiting InAs/AlAs Colloidal Quantum dots*. IEEE Access. (2024). [Online]. Available: https://ieeexplore.ieee.org/abstract/document/10669954

[45] S. Matloub, A. Eftekhari, and A. Rostami. *Highly ultra-broadband QD-SOA exploiting superimposition of quantum dots*. J. Mod. Opt. vol. 69, no. 2. (Jan. 2022). pp. 92–102. doi: 10.1080/09500340.2021.2002449.

[46] F. Hakimian, M. R. Shayesteh, and M. R. Moslemi. *Proposal for Modeling of FWM Efficiency of QD-SOA Based on the Pump/Probe Measurement Technique*. J. Optoelectron. Nanostructures. vol. 5, no. 4. (2020). pp. 49–66. [Online]. Available: https://sanad.iau.ir/en/Article/1182873

[47] H. Dortaj, M. Faraji, and S. Matloub. *High-speed and high-contrast two-channel all-optical modulator based on solution-processed CdSe/ZnS quantum dots*. Sci. Rep. vol. 12, no. 1. (Jul. 2022). p. 12778. doi: 10.1038/s41598-022-17084-4.

[48] H.-Y. Chiu, V. Perebeinos, Y.-M. Lin, and P. Avouris. *Controllable pn junction formation in monolayer graphene using electrostatic substrate engineering*. Nano Lett. vol. 10, no. 11. (2010). pp. 4634–4639. [Online]. Available: https://pubs.acs.org/doi/abs/10.1021/nl102756r

[49] B. Brar, G. D. Wilk, and A. C. Seabaugh. *Direct extraction of the electron tunneling effective mass in ultrathin SiO2*. Appl. Phys. Lett. vol. 69, no. 18. (1996). pp. 2728–2730. [Online]. Available: https://pubs.aip.org/aip/apl/article-abstract/69/18/2728/66656

[50] R. Kumar Chanana. *Determination of hole effective mass in SiO2 and SiC conduction band offset using Fowler–Nordheim tunneling characteristics across metal-oxide-semiconductor structures after applying oxide field corrections*. J. Appl. Phys. vol. 109, no. 10. (2011). p. 104508. [Online]. Available: https://pubs.aip.org/aip/jap/article-abstract/109/10/104508/985206/Determination-of-hole-effective-mass-in-SiO2-and?redirectedFrom=fulltext

[51] H. Chen, X. Sun, K. W. C. Lai, M. Meyyappan, and N. Xi. *Infrared detection using an InSb nanowire*. in 2009 IEEE Nanotechnology Materials and

Devices Conference, IEEE. (2009). pp. 212–216. [Online]. Available: https://ieeexplore.ieee.org/abstract/document/5167558/
[52] J. Piprek. *Semiconductor optoelectronic devices: introduction to physics and simulation*. Elsevier. (2013).
[53] R. Debnath, O. Bakr, and E. H. Sargent. *Solution-processed colloidal quantum dot photovoltaics: A perspective*. Energy Environ. Sci. vol. 4, no. 12. (Nov. 2011). p. 4870. doi: 10.1039/c1ee02279b.
[54] M. Yuan, M. Liu, and E. H. Sargent. *Colloidal quantum dot solids for solution-processed solar cells*. Nat. Energy. vol. 1, no. 3. (Feb. 2016). p. 16016. doi: 10.1038/nenergy.2016.16.
[55] F. P. García de Arquer, A. Armin, P. Meredith, and E. H. Sargent. *Solution-processed semiconductors for next-generation photodetectors*. Nat. Rev. Mater. vol. 2, no. 3. (Jan. 2017). p. 16100. doi: 10.1038/natrevmats.2016.100.
[56] K. Safari Anzabi, A. Habibzadeh-Sharif, M. J. Connelly, and A. Rostami. *Wideband Steady-State and Pulse Propagation Modeling of a Reflective Quantum-Dot Semiconductor Optical Amplifier*. J. Light. Technol. vol. 38, no. 4. (Feb. 2020). pp. 797–803. doi: 10.1109/JLT.2019.2947648.
[57] J. Kim, C. Meuer, D. Bimberg, and G. Eisenstein. *Effect of Inhomogeneous Broadening on Gain and Phase Recovery of Quantum-Dot Semiconductor Optical Amplifiers*. IEEE J. Quantum Electron. vol. 46, no. 11. (Nov. 2010). pp. 1670–1680. doi: 10.1109/JQE.2010.2058793.
[58] Dortaj, Hannaneh, and Samiye Matloub. *Design and modeling of multi-color absorber based on periodic van der Waals heterostructures including TMDCs*. Journal of Computational Electronics 24.2 (2025). p. 64, https://doi.org/10.1007/s10825-025-02304-7.
[59] F. Demangeot, D. Simeonov, A. Dussaigne, R. Butté, and N. Grandjean. *Homogeneous and inhomogeneous linewidth broadening of single polar GaN/AlN quantum dots*. Phys. status solidi c. vol. 6, no. S2. (Jun. 2009). pp. S598–S601. doi: 10.1002/pssc.200880971.
[60] J. Jasieniak, L. Smith, J. van Embden, P. Mulvaney, and M. Califano. *Re-examination of the Size-Dependent Absorption Properties of CdSe Quantum Dots*. J. Phys. Chem. C. vol. 113, no. 45. (Nov. 2009). pp. 19468–19474. doi: 10.1021/jp906827m.
[61] J. R. Lakowicz. *Principles of Fluorescence Spectroscopy*. Boston, MA, MA: Springer US. (2006). doi: 10.1007/978-0-387-46312-4.
[62] R. Wang, R. S. Deacon, D. Car, E. Bakkers, and K. Ishibashi. *InSb nanowire double quantum dots coupled to a superconducting microwave cavity*. Appl. Phys. Lett. vol. 108, no. 20. (2016). p. 203502. [Online]. Available: https://pubs.aip.org/aip/apl/article-abstract/108/20/203502/31054/InSb-

nanowire-double-quantum-dots-coupled-to-a?redirectedFrom=fulltext
[63] D. E. Aspnes and A. A. Studna. *Dielectric functions and optical parameters of si, ge, gap, gaas, gasb, inp, inas, and insb from 1.5 to 6.0 ev*. Phys. Rev. B. vol. 27, no. 2. (1983). p. 985. [Online]. Available: https://journals.aps.org/prb/abstract/10.1103/PhysRevB.27.985
[64] M. Y. Gubin, A. V Shesterikov, A. V Prokhorov, and V. S. Volkov. *Hybrid schemes for excitation of collective resonances with surface plasmon polaritons in arrays of quantum dots in the proximity of graphene*. Laser Photon. Rev. vol. 14, no. 12. (2020). p. 2000237. [Online]. Available: https://onlinelibrary.wiley.com/doi/abs/10.1002/lpor.202000237
[65] K. Sebald *et al. Optical Gain of CdSe Quantum Dot Stacks*. Phys. status solidi. vol. 190, no. 2. (Apr. 2002). pp. 593–597. doi: 10.1002/1521-396X(200204)190:2<593::AID-PSSA593>3.0.CO;2-4.
[66] D. Bimberg, M. Grundmann, and N. N. Ledentsov. *Quantum Dot Heterostructures*. John Wiley. (1998).
[67] A. Shen *et al. Low confinement factor quantum dash (QD) mode-locked Fabry-Perot (FP) laser diode for tunable pulse generation*. in OFC/NFOEC 2008 - 2008 Conference on Optical Fiber Communication/National Fiber Optic Engineers Conference, IEEE. (Feb. 2008). pp. 1–3. doi: 10.1109/OFC.2008.4528481.
[68] M. Mohamadzadeh, S. Matloub, and M. Faraji. *Simulation and design of dual-wavelength all-optical semiconductor optical amplifier with solution-processed quantum dots*. Opt. Mater. (Amst). vol. 150. (2024). p. 115230. [Online]. Available: https://www.sciencedirect.com/science/article/abs/pii/S0925346724004130